crystals

MDPI

Article

The Comparison of Microstructure, Phase Composition and Mechanical Properties of Inconel 625 Alloys Obtained by Wire Arc and Wire Electron Beam Additive Manufacturing

Denis Gurianov *, Sergey Fortuna, Sergei Tarasov *, Vyacheslav Semenchuk, Nikolay Shamarin, Andrey Chumaevskii, Valery Rubtsov, Alexander M. Korsunsky and Evgeny Kolubaev

Institute of Strength Physics and Materials Science, Siberian Branch of Russian Academy of Sciences, 634055 Tomsk, Russia; s_fortuna@ispms.tsc.ru (S.F.); svm_70@ispms.ru (V.S.); shnn@ispms.ru (N.S.); tch7av@ispms.ru (A.C.); rvy@ispms.ru (V.R.); korsunskijam@mai.ru (A.M.K.); eak@ispms.ru (E.K.)
* Correspondence: gurianov@ispms.ru (D.G.); tsy@ispms.ru (S.T.)

Abstract

The present paper compares the microstructure and mechanical properties of Inconel 625 alloy samples produced by using wire-arc additive manufacturing (WAAM) and wire electron beam additive manufacturing (WEBAM). The obtained wall-shaped samples did not contain any macroscopic defects in the form of cracks, delaminations and geometry distortions. The WAAM-built "wall" exhibits finer dendritic structures (WAAM—10–16 μm; WEBAM—20–25 μm). Also, the WAAM-built one is characterized by the more homogeneous-sized distribution of microstructure components. In both cases, the material is represented by the γ-phase, with large precipitates of MC-type carbides in the interdendritic spaces. Additionally, the sample obtained using the WAAM contained aluminum oxide. It was found that the intrinsic periodic heat treatment is not sufficient for the formation of the γ″-phase, and it is necessary to perform a subsequent long-term aging. However, the overall mechanical properties of both samples show similar levels of yield stress and ultimate tensile strength, and demonstrate the same degree of anisotropy.

Keywords: additive manufacturing; wire arc; electron beam; superalloy; Inconel 625

Academic Editor: Qian Lei

Received: 18 August 2025
Revised: 15 September 2025
Accepted: 26 September 2025
Published: 29 September 2025

Citation: Gurianov, D.; Fortuna, S.; Tarasov, S.; Semenchuk, V.; Shamarin, N.; Chumaevskii, A.; Rubtsov, V.; Korsunsky, A.M.; Kolubaev, E. The Comparison of Microstructure, Phase Composition and Mechanical Properties of Inconel 625 Alloys Obtained by Wire Arc and Wire Electron Beam Additive Manufacturing. *Crystals* **2025**, *15*, 848. https://doi.org/10.3390/cryst15100848

1. Introduction

Inconel 625 (IN625) superalloy is a material finding wide use for manufacturing critical parts of aircraft and electric power generating turbines, rocket engines, furnaces, marine systems and nuclear power plants, etc. These applications require operating under high-temperature, extreme loading conditions, which call for high resistance to creep and corrosion. The class of superalloys to which IN625 belongs offers a combination of the required high-temperature properties, including high strength, high resistance to creep and fatigue and resistance to oxidation and corrosion in aggressive environments [1–6]. All these characteristics appear due to the microstructures obtained by alloying a nickel-chromium solid solution with Mo, Nb and Fe, and this leads to the formation of several component phases. The addition of molybdenum and niobium provides solid–solution hardening of the nickel-chromium matrix (γ-phase) as well as the formation of corresponding carbides, which contribute to grain boundary immobilization and thus prevent the grain boundary slip [1–3]. In addition, niobium is necessary for the precipitation of an intermetallic reinforcement γ″-phase (Ni_3Nb), which has an ordered body-centered tetragonal lattice with a D022 superstructure [6]. However, the same elements can also form

undesirable, brittle and topologically close packed (TCP) phases: σ (FeCr, FeCrMo, CrCo), μ and Laves phases. The TCP phases are formed from carbides such as MC, M_6C and $M_{23}C_6$ during a long-term exposure to high temperatures and adversely affect the alloy mechanical properties, especially its creep resistance [1,6].

In the structural phase state that provides the required operational characteristics, the mechanical properties of Inconel 625 alloy reach the following values: yield strength—1000–1300 MPa; tensile strength—1300–1400 MPa; and elongation—21–45%. Such properties are achieved with a structure containing equiaxed grains with a uniform distribution of alloying elements and an optimal content of the phases described above. To obtain this structure, a multistage heat treatment is required, which includes homogenization (~1200 °C for ~2–4 h) and aging (~580–760 °C for ~8 h).

Traditional methods of manufacturing superalloy components demonstrate low productivity due to the requirement of multi-step workpiece preparation, rapid wear of the cutting tools and a vast amount of waste [1,3,4]. As an alternative to traditional methods, additive manufacturing technologies are needed for increasing productivity and reducing manufacturing costs [1,7]. Additive manufacturing uses compact and concentrated high-energy thermal sources in the form of laser beams, electron beams and electric arc discharges for melting and layer-by-layer deposition of feedstock material on a substrate [2]. Materials produced by additive methods are usually characterized by the anisotropy of their mechanical properties stemming from directional solidification of dendritic (columnar) structures [5]. For the majority of applications, the directional solidification and corresponding anisotropy are detrimental and should be eliminated by means of some post-treatment. However, it is also known that it may be used for the benefit of improving the creep characteristics of the superalloys. In order to fabricate components with a preferred crystallographic orientation of grains (texture), directional solidification methods are used, which are characterized by a high-temperature gradient at a moving solidification front. An additive process is characterized by high heating and cooling rates reaching 10^8 K/s. The molten pool created by the above-mentioned energy sources serves to significantly increase the temperature gradient in comparison with that of traditional casting and raise its value to 10^6 K/m [3]. This, in turn, determines the size and morphology of the structural and phase components that affect the operational characteristics [2].

One of the modern additive manufacturing methods is a wire feed electron beam additive manufacturing (WEBAM). The average deposition rate and layer thickness achieved in the WEBAM are about 20 kg/h and 3 mm, respectively [8]. The WEBAM process is also suitable for producing large-sized parts that present a challenge for powder-bed methods such as SLM. WEBAM is conducted in a vacuum chamber, which allows for eliminating problems with oxidation and contamination. Other advantages include high energy density, adjustment of electron beam current (heat input) and electron beam scanning for controlling the molten pool size and shape. The typical wire diameter for WEBAM is between 0.5 mm and 3.0 mm, allowing the system to be used flexibly to form parts of complex shapes [8]. Also, the process allows manufacturing products from various metals and alloys (including wires of dissimilar metals) with different dimensions, mechanical and performance characteristics.

Currently, when considering the production of parts from nickel-based superalloys by electron beam technology, the powder-bed approach is most often used [9–11]. Publications addressing additive deposition from either wire or rod are found lacking in the modern literature [12–15].

Wire Arc Additive Manufacturing (WAAM) is a widely used process that allows for the restoring or near-net-shape building of large and shaped machine parts [16]. Similar to any additive method, WAAM is designed to reduce the time and cost of obtaining products

due to the greater deposition rate and reduced material waste [3,16–20]. The application of this technique to Inconel 625 alloy is readily found in the current literature. Recently, it was shown [16] that WAAM allows obtaining functional gradient materials from Inconel 625 and stainless steel ASTM 321. Other researchers [17] studied the improvement of corrosion resistance of WAAM-built Inconel 625 alloy samples by aluminization. This method allows for about 6-fold improvement in the resistance to high-temperature corrosion. One of the main disadvantages of the wire additive technologies is that the as-built components have high waviness and roughness of the surfaces, as compared to those obtained from powder-bed methods. Therefore, greater machining allowances are required for the wire additively manufactured items. Electric discharge machining is the most suitable method for cutting them to size [18].

While a significant number of publications are devoted to WAAM of Inconel 625, those devoted to WEBAM of Inconel 625 are scarce. In this regard, the purpose of the present work is to compare the structural characteristics and mechanical properties of Inconel 625 samples obtained by WAAM and WEBAM and draw conclusions regarding the suitability and preferability of each of these two methods for specific applications.

2. Materials and Methods

The feedstock Inconel 625 wire had a diameter of 1.2 mm. The elemental composition of the wire (Table 1) was determined by X-ray fluorescence analysis using a Niton XL3t GOLDD instrument (Thermo Fisher Scientific, Waltham, MA, USA). The experimental WEBAM machine was developed in-house at the Institute for Strength Physics and Materials Science, Siberian Branch of the Russian Academy of Sciences (ISPMS SB RAS, Tomsk, Russia) [21,22]. The WAAM equipment included a FANUC robot ARC Mate 100iD (FANUC Europe Corporation, Luxemburg) and an EWM Titan XQ R 400 Pulse inverter power supply welding machine (EWM GmbH, Mundersbach, Germany).

Table 1. Chemical composition of the raw wire of Inconel 625 alloy.

Ni	Cr	Mo	Nb	Fe	C *	Al	Ti	Co	Mn + Si + S + P
58.63	21.7	8.78	3.95	4.5	-	0.2	0.19	0.95	1.1

* Carbon content is not determined by XRF.

In both cases, 5 mm thick hot-rolled stainless steel plates were used as substrates. The samples in the form of 120 × 51 × 6.8 mm^3 and 120 × 57 × 6.4 mm^3 walls were obtained using WEBAM and WAAM, respectively. Each was composed of 50 successively deposited layers. In both cases, the Inconel 625 alloy wire was fed into the focus of a heat source (electron beam or arc), melted and transferred to the melt pool. The worktable was moved according to the prescribed algorithm to form an additive layer of material. The reciprocating path deposition strategy was used in both cases. The process regimes under which the samples and process schemes were obtained are summarized in Table 2 and Figure 1, respectively. It should be noted that the electron beam current was reduced progressively as the height of the built wall-shaped sample increased. Such a current decay was necessary to avoid metal spilling in the top part of the wall. In the case of WAAM, the arc current was constant.

Table 2. Technological parameters of additive processes used in obtaining samples from Inconel 625 alloy.

Additive Process	Current, A	Accelerating Voltage, V	Printing Velocity, mm/min	Heat Input, kJ/mm	Environment
WEBAM	43×10^{-3}–27×10^{-3}	30×10^{3}	220	0.35–0.22	Vacuum
WAAM	111	17.4	500	0.23	Argon

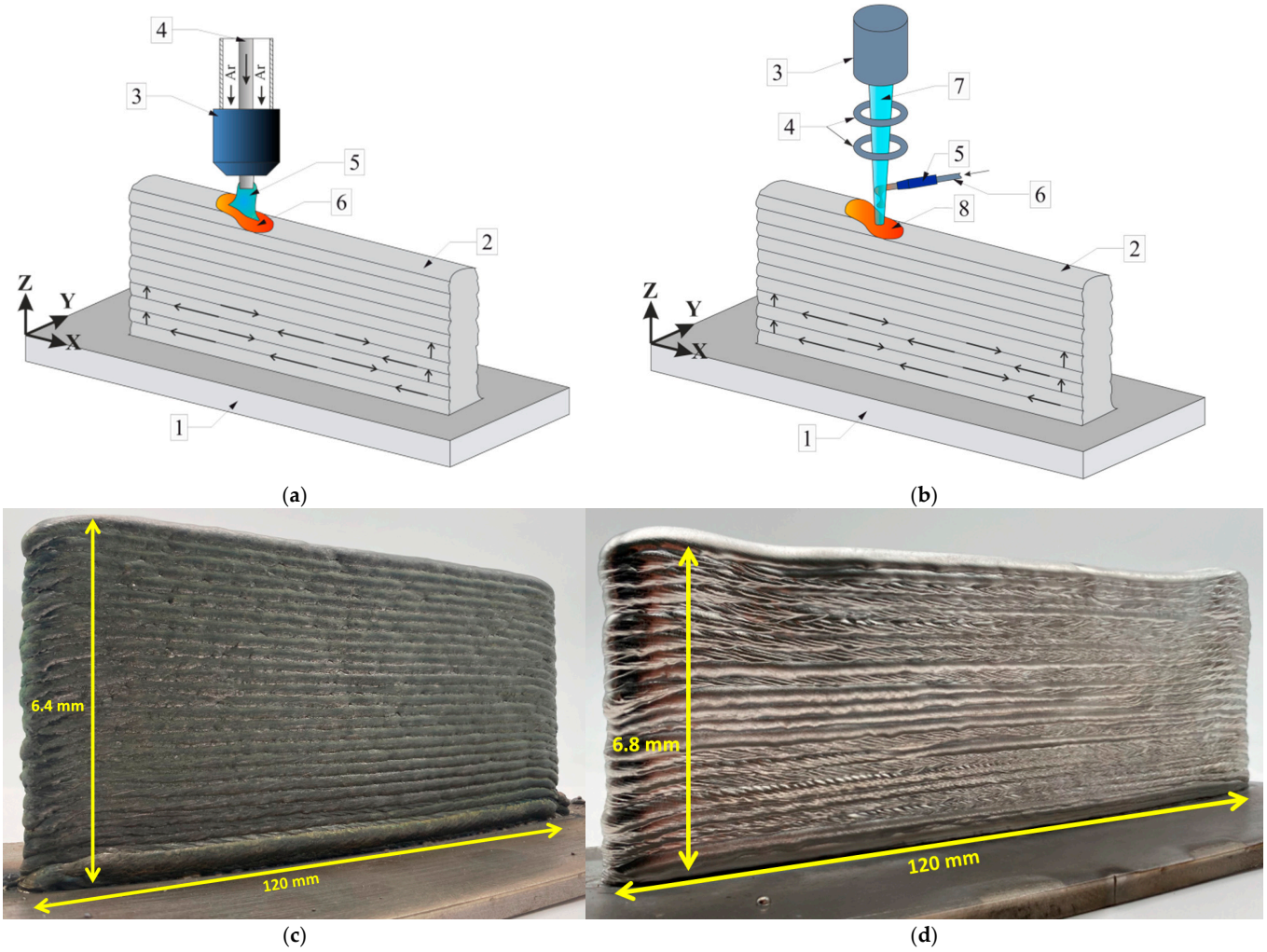

Figure 1. (**a**)—Schematic diagram of WAAM process: 1—steel substrate, 2—additively formed sample, 3—welding torch, 4—source wire, 5—welding arc, 6—molten pool; (**b**)—schematic diagram of WEBAM process: 1—steel substrate, 2—additively formed sample, 3—electron gun, 4—focusing system, 5—wire feeding system, 6—source wire, 7—electron beam, 8—molten pool; (**c**)—general view of the sample obtained by WAAM; (**d**)—general view of the sample obtained by WEBAM.

To obtain specimens for metallographic studies, samples were cut into longitudinal sections and were ground and polished, followed by chemical etching in Marble's reagent ($CuSO_4$—10 g, HCl—50 mL, H_2O—50 mL). Metallographic studies were performed using an OLS LEXT 4100 laser confocal microscope (OLYMPUS Corporation, Tokyo, Japan). A LEO EVO 50 scanning electron microscope (SEM) (Carl Zeiss, Oberkochen, Germany) was used for microstructural studies. A JEOL JEM-2100 transmission electron microscope (TEM) (Tokyo Boeki Ltd., Tokyo, Japan) was used for fine structure studies and phase composition identification. Mechanical testing of the samples was carried out on a UTS-110M testing machine (Testsystems, Ivanovo, Russia) by uniaxial quasistatic tension. Samples for mechanical testing were cut off the walls so that their tensile axes coincided with either

(i) layer deposition direction (X axis) or (ii) building direction (Z axis). The gauge part of the tested samples was 12 mm with a cross-section of 3 × 3 mm. Static tensile tests were carried out at room temperature at a rate of 1 mm/min.

3. Results and Discussions

An investigation of the macrostructure revealed the following features. The use of reciprocating path deposition strategy in both additive processes is anticipated to give rise to the formation of zigzag grain structures [22]. However, the presence of such a zigzag structure was only observed through the fifth and second initial deposited layers in WEBAM (Figure 2a) and WAAM (Figure 2b), respectively. The majority of the material is composed of directionally growing primary dendrite arms with weakly developed secondary arms (Figure 2c,d). The mean angle of inclination of dendritic axes growth toward the deposition path direction was found to be 79.7 ± 1.4° for WAAM and 77.6 ± 1.7° for WEBAM. It is noteworthy that in both cases, there was no observed tendency for the dendrite growth angle to change as the height of the additively formed samples increased. Additionally, no macroscopic defects in the form of pores or cracks were detected.

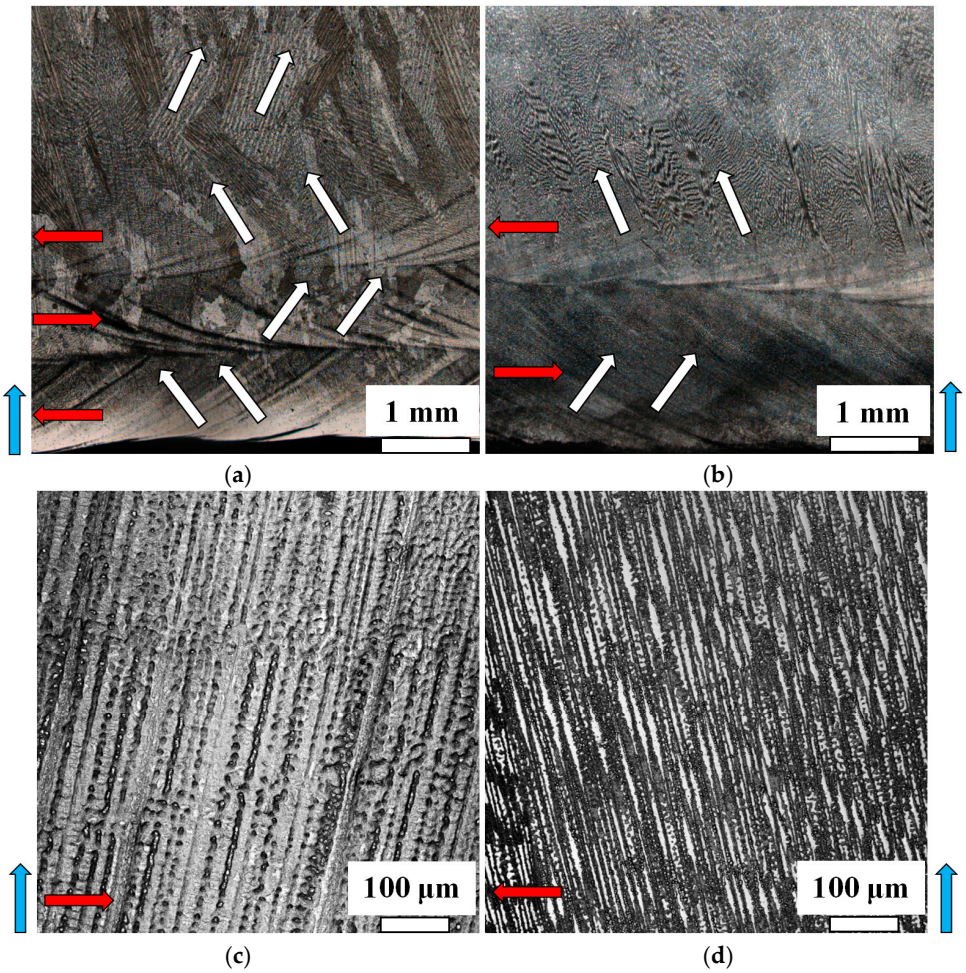

Figure 2. (**a**,**c**)—Macro and microstructure of Inconel 625 alloy after WEBAM; (**b**,**d**)—macro and microstructure of Inconel 625 alloy after WAAM. White arrows indicate the direction of dendritic colonies growth. Red arrows indicate the direction of electron scanning trajectory. Blue arrows indicate the additive building direction.

Dendritic structures are characterized by the average primary dendrite arm spacing (PDAS), which enables the assessment of alterations in solidification conditions across a range of technological processes involving material melting. Table 3 and Figure 3 provide

a summary of the PDAS values for the sample material obtained using two additive technologies. As evidenced by the presented data, an increase in PDAS is observed in both cases as the height of the formed samples increases. This is associated with a decrease in the value of the temperature gradient, which can be attributed to the accumulation of heat in the underlying additively deposited layers that have already undergone solidification. Furthermore, it can be observed that in the case of WAAM, the PDAS is smaller than in the case of WEBAM, with a value that is almost twice as high over the entire height of the additively deposited product. Moreover, the reliability of the linear approximation in the case of WAAM is higher (R^2 = 0.65) than in the case of WEBAM (R^2 = 0.60).

Table 3. Average PDAS values (μm) in different areas of the samples.

Additive Process	Bottom	Middle	Top
WEBAM	20.3 ± 2.7	24.1 ± 1.1	25.2 ± 0.9
WAAM	10.0 ± 0.6	10.6 ± 3.3	16.5 ± 1.4

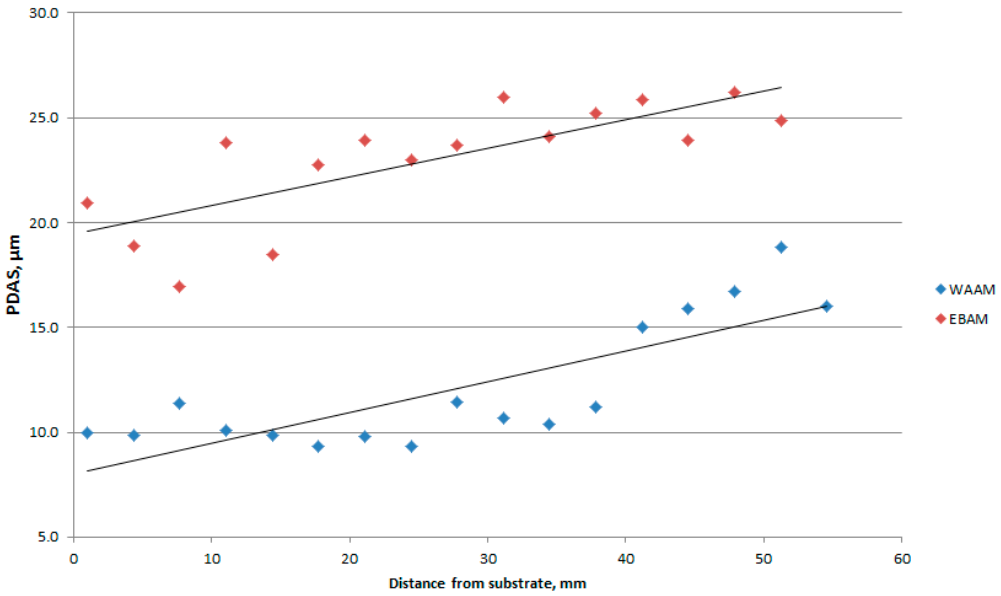

Figure 3. Changes in the average primary dendrite arm spacing (PDAS) as a function of the height of additively obtained samples.

Using the Kurz–Fisher model [23], which predicts PDAS, one can solve the inverse problem and estimate changes in the magnitude of the temperature gradient G (K/m) based on previously obtained PDAS data:

$$G = \left(\frac{\lambda}{A \times R^{-0.25}} \right)^{-2} \quad (1)$$

where λ is PDAS; R is the crystallization rate, taken as the speed of moving the working table; and A is the Gibbs–Thomson coefficient (3.65×10^{-7} K·m). The equilibrium freezing range is (60 K), the liquid diffusion coefficient is (3×10^{-9} m^2 s^{-1}) and the equilibrium partition coefficient is (0.48) [23]. The data from Tables 2 and 3 were substituted into expression (1), resulting in the average values of the temperature gradient for the samples obtained by the two additive technologies (Table 4). The results demonstrate that the temperature gradient magnitude is significantly higher in the WAAM samples compared to the WEBAM samples. In the bottom part of the samples, the gradient is approximately 2.6 times higher in WAAM compared to WEBAM. Similarly, in the middle part of the

samples, the gradient is approximately 3.5 times higher in WAAM compared to WEBAM. Finally, in the top part of the samples, the gradient is approximately 1.6 times higher in WAAM compared to WEBAM. In contrast, the temperature gradient alterations observed in the WEBAM samples are more uniform, suggesting a more stable solidification process and, consequently, a more homogeneous formed structure.

Table 4. Average G values (given in K/cm) in different areas of the samples.

Additive Process	Bottom	Middle	Top
WEBAM	155.0 ± 40.3	105.2 ± 9.3	96.4 ± 6.9
WAAM	405.9 ± 47.4	366.6 ± 62.4	154.6 ± 23.89

SEM studies of the microstructure revealed the presence of secondary phases exclusively within the interdendritic space (Figure 4). The secondary phases were identified as belonging to two distinct categories: niobium-enriched and niobium-titanium-enriched ones. This observation was made in both the WAAM and WEBAM samples. It seems reasonable to conclude that these phases are the MC-type carbides. It is also noteworthy that the WAAM sample exhibited the presence of aluminum-enriched particles. Furthermore, evidence of dendritic partitioning of chemical elements was observed. Therefore, niobium is nearly undetectable in the dendritic arms, whereas its concentration in the interdendritic space is approximately 8 wt.% (for both WAAM and WEBAM). A comparable pattern of behavior is observed in the case of molybdenum. In the dendrite arms, its content is approximately 7–9 wt.%, and in the interdendritic space, it is approximately 11–12 wt.%. The two additive processes to create the samples from the Inconel 625 alloy were carried out on steel substrates. This inevitably results in a change to the chemical composition of the material formed near the substrate due to the intermixing. It was determined that the chemical composition aligns with the specified grade composition at a depth of approximately 5 mm for both WAAM and WEBAM.

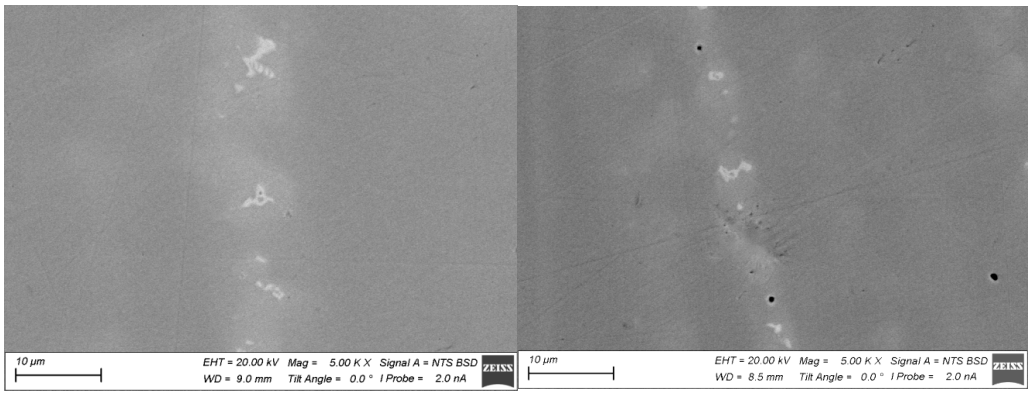

(**a**) (**b**)

Figure 4. Microstructure of Inconel 625 alloy after WEBAM (**a**) and WAAM (**b**).

To obtain a more accurate identification of the phase composition and fine structure, TEM studies were conducted. The fine structure of the WEBAM Inconel 625 alloy is represented by the γ-phase and MC-type carbides of irregular shape (Figures 5 and 6). The results of the EDS analysis (Table 5) and the interpretation of the corresponding SAED patterns indicate the presence of carbides with two distinct compositions: NbC and (Nb, Ti) C. Additionally, NbC carbides are observed to form near titanium-containing carbides. The structural phase composition of the WAAM Inconel 625 alloy is also represented by a γ-phase matrix and carbides of two types, similar to those in the WEBAM sample. Additionally, the presence of aluminum oxide precipitates with a size range of 0.4 to 1 µm

was observed (Figures 7 and 8). Despite using argon shielding in WAAM, the formation of Al_2O_3 remains a possibility. Following both additive processes, the carbides exhibited an irregularly elongated morphology with dimensions of 0.8 to 2.2 µm and 0.4 to 0.8 µm in the cases of WEBAM and WAAM, respectively.

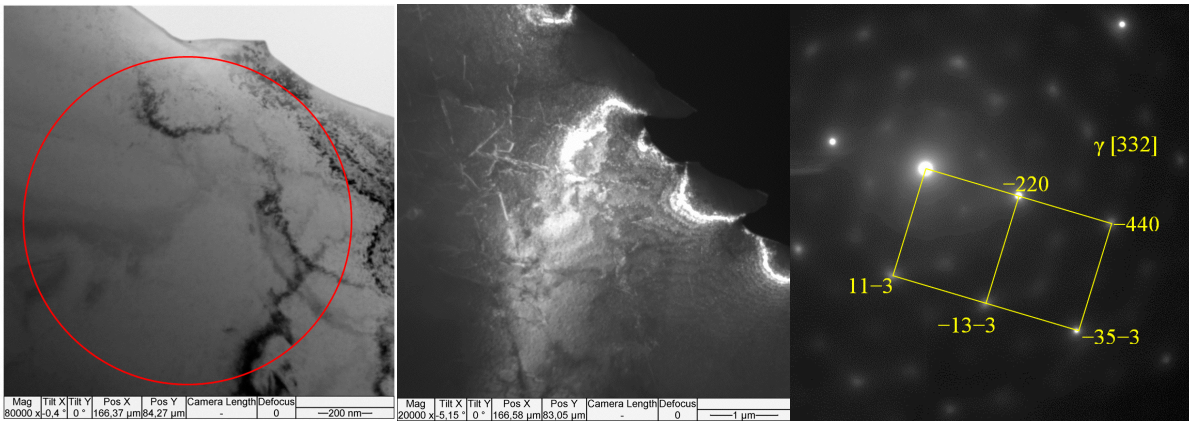

(**a**) (**b**) (**c**)

Figure 5. WEBAM sample TEM bright field (**a**) and dark field (**b**) images. The SAED pattern (**c**) is obtained from the region highlighted by the red circle in figure (**a**). The dark-field image is obtained in the reflection -220_{γ}.

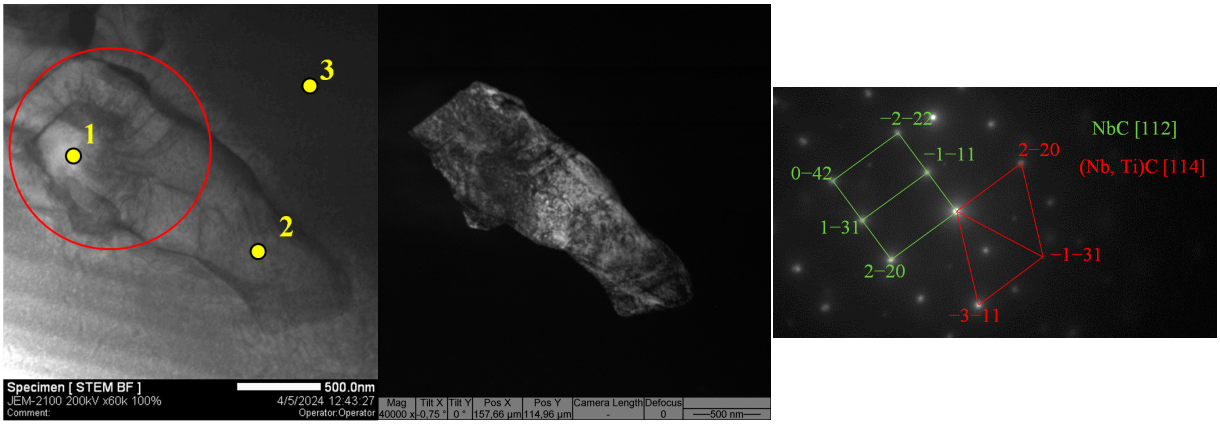

(**a**) (**b**) (**c**)

Figure 6. WEBAM sample TEM bright-field STEM (**a**) and dark-field (**b**) images. The SAED pattern (**c**) is obtained from the region highlighted by the red circle in figure (**a**). The dark-field image is obtained in the closely spaced $2–20_{NbC}$ and $-220_{(Nb,\,Ti)\,C}$ reflections.

Table 5. Chemical composition of structural elements identified in Figures 6–8, at %.

Additive Technology	EDS Probe (Figures 6–8)	Phase	Al	Ti	Cr	Fe	Co	Ni	Nb	Mo	O
WEBAM	1	MC	0.01	41.73	3.42	0.53	0.38	5.82	47.14	1.09	-
	2	MC	-	2.71	2.25	0.67	0.55	5.14	85.81	2.75	-
	3	γ	0.05	0.15	19.62	0.74	0.40	63.03	6.60	8.99	-
WAAM	4	Al_2O_3	28.28	-	0.38	-	-	0.68	-	-	70.66
	5	γ	0.34	0.03	26.80	0.63	0.44	62.92	1.69	7.17	-
	6	Al_2O_3	25.06	-	2.02	-	-	5.56	-	-	67.38
	7	MC	-	28.48	6.66	0.63	0.02	11.33	54.19	-	-
	8	γ	0.46	0.02	23.61	0.48	0.15	62.49	4.46	8.36	-
	9	MC	-	1.64	7.52	0.18	0.01	15.25	68.45	7.28	-

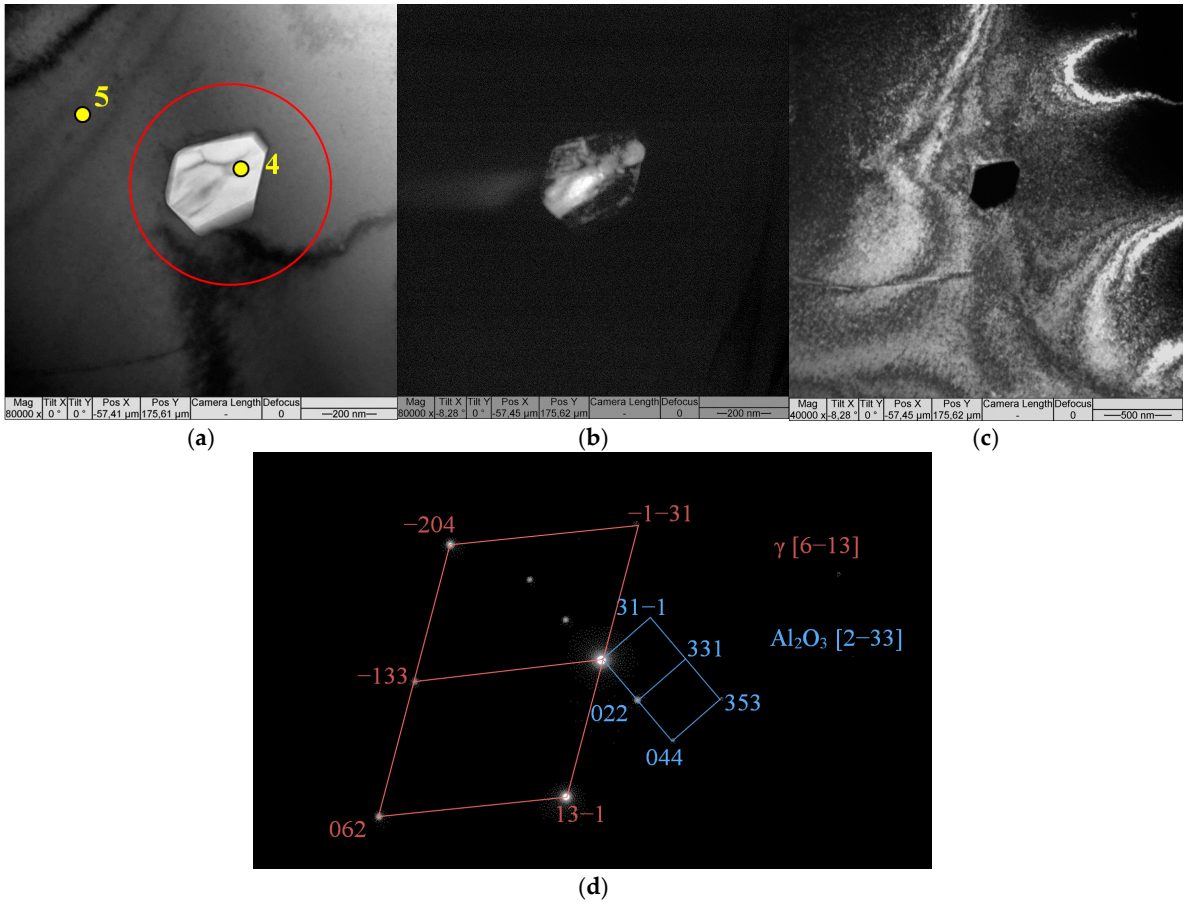

Figure 7. WAAM sample TEM bright-field (**a**) and dark-field (**b**,**c**) images. The SAED pattern (**d**) is obtained from the region highlighted by the red circle in figure (**a**). Dark-field images are obtained in $13\text{-}1_{\gamma}$ and 022_{Al2O3} reflections.

The TEM examination did not allow to identify the presence of either γ′ or γ″- phases in both WEBAM and WAAM samples. This is due to the fact that the formation of these phases necessitates long thermal treatment, including aging, which must be conducted over a period of several tens of hours [24–27]. Similarly, the precipitation of the Laves phase and the δ phase is precluded by the aforementioned circumstances.

Table 6 illustrates the mechanical properties of the WEBAM and WAAM Inconel 625 alloy samples. As can be observed in both cases, the properties differ depending on the tensile axis orientation with respect to the wall height and length. Therefore, the samples with tensile axis along the layer deposition direction (X axis) exhibit higher values of both yield strength and relative elongation. This phenomenon can be attributed to the fact that in this case, the direction of dendrite arms growth is perpendicular to the tensile axis of the samples, which contributes to the plasticity of the material. It is noteworthy that the samples obtained through different additive processes exhibit minimal variation in mechanical properties.

Despite the differences in PDAS, the mechanical properties of WAAM and EBAM samples are at the same level. In the "as-deposited" state, dispersion strengthening due to the precipitation of the γ″ phase and fine dispersed carbides is not realized. In both cases, the material is represented by the γ-phase, providing only a solid–solution strengthening, while large precipitates of carbides do not contribute to the strengthening of the material.

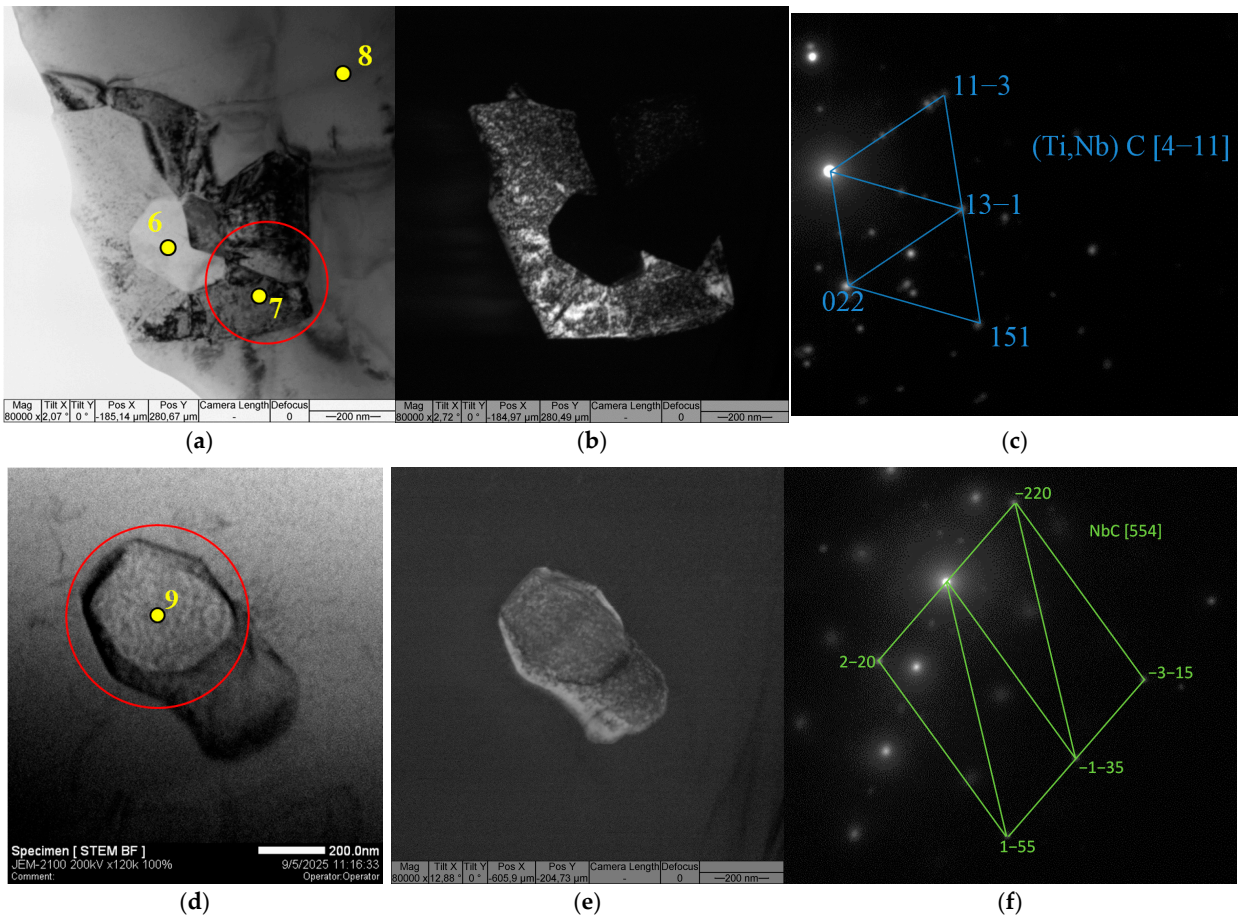

Figure 8. WAAM sample TEM bright-field (**a**), STEM bright-field (**d**) and dark-field (**b**), (**e**) images. The SAED patterns (**c**) and (**f**) are obtained from the region highlighted by the red circle in figures (**a**), (**d**), respectively. The dark-field image (**b**) is obtained in reflection $022_{(Nb,\,Ti)\,C}$. The dark-field image (**e**) is obtained in reflection $2–20_{NbC}$.

Table 6. Mechanical properties of Inconel 625 after WEBAM and WAAM processes.

Additive Process	Direction of Samples Cutting	UTS, MPa	YS, MPa	δ, %
WEBAM	Vertical	644 ± 44	343 ± 35	72 ± 3
	Horizontal	649 ± 37	563 ± 19	109 ± 3
WAAM	Vertical	625 ± 8	327 ± 6	71 ± 4
	Horizontal	652 ± 19	536 ± 14	104 ± 1

Despite the absence of undesirable, brittle and topologically close packed phases, the mechanical properties of the obtained samples are lower than those of the heat-treated material [27–30], which is primarily due to the absence of the reinforcing γ''-phase.

4. Conclusions

In the course of the present study, defect-free samples in the form of thin walls of Inconel 625 alloy were produced by two additive technologies WAAM and WEBAM. It was found that the macrostructure is represented by directionally growing dendrites despite using the multidirectional printing path. The primary dendrite arm spacing in the case of WEBAM is 20–25 μm, and in the case of WAAM 10–16 μm, which indicates a greater value of the temperature gradient inside the WAAM molten pool. In the material of samples

obtained by each additive process, no formation of either TCP embrittlement phases or reinforcement γ''- and δ-phases was observed due to the rapidity of the solidification processes inherent in these methods and due to the insufficient intrinsic heat treatment. To solve this problem, it is possible to adapt the deposition regimes to achieve a slower deposition rate whilst keeping the same beam current. It is noted that the presence of argon shielding during the WAAM process does not completely prevent the formation of oxides. When comparing the mechanical properties, no significant differences were found between the samples obtained by WAAM and WEBAM methods, and the degree of anisotropy of properties in both cases is similar.

Author Contributions: Conceptualization, A.C. and V.R.; methodology, D.G.; validation, S.F. and S.T.; formal analysis, D.G.; investigation, V.S. and N.S.; resources, V.R.; data curation, A.C.; writing—original draft preparation, D.G.; writing—review and editing, S.T., S.F., A.C. and A.M.K.; supervision, E.K.; project administration, E.K.; funding acquisition, E.K. All authors have read and agreed to the published version of the manuscript.

Funding: This study was carried out under the Agreement for the provision of grant funding from the federal budget for large scientific projects in priority areas of scientific and technological development of the Russian Ministry of Science and Higher Education № 075-15-2024-552.

Data Availability Statement: Dataset available on request from authors.

Acknowledgments: The investigations were carried out using the equipment of Shared Use Centre "Nanotech" of the ISPMS SB RAS.

Conflicts of Interest: The authors declare no conflicts of interest.

References

1. Ferreira, A.A.; Reis, A.R.; Amaral, R.L.; Cruz, J.M.; Romio, P.C.; Seabra, J.O.; Vieira, M.F. Mechanical and microstructural characterisation of bulk Inconel 625 produced by direct laser deposition. *Mater. Sci. Eng. A* **2022**, *838*, 142777. [CrossRef]
2. Li, J.; Yao, J.; Zhao, G.; Li, H.; Li, Y.; Liu, J. The Influence of Different Focusing Currents on the Microstructure Evolution and Wear Properties of a Scanning Electron Beam Modified Inconel 625 Nickel Base Alloy Surface. *Crystals* **2023**, *13*, 325. [CrossRef]
3. Shahwaz, M.; Nath, P.; Sen, I. A critical review on the microstructure and mechanical properties correlation of additively manufactured nickel-based superalloys. *J. Alloys Compd.* **2022**, *907*, 164530. [CrossRef]
4. Zafar, F.; Emadinia, O.; Conceição, J.; Vieira, M.; Reis, A. A Review on Direct Laser Deposition of Inconel 625 and Inconel 625-Based Composites—Challenges and Prospects. *Metals* **2023**, *13*, 787. [CrossRef]
5. Schmeiser, F.; Krohmer, E.; Wagner, C.; Schell, N.; Uhlmann, E.; Reimers, W. In situ microstructure analysis of Inconel 625 during laser powder bed fusion. *J. Mater. Sci.* **2022**, *57*, 9663–9677. [CrossRef]
6. Wang, F.; Liu, H.; Li, J.; Wan, H.; Yu, L.; Liu, B. Microstructure Evolution and Mechanical Properties of Inconel 625 Foils. *J. Mater. Eng. Perform.* **2023**, *32*, 6576–6587. [CrossRef]
7. Poulin, J.-R.; Kreitcberg, A.; Brailovski, V. Effect of hot isostatic pressing of laser powder bed fused Inconel 625 with purposely induced defects on the residual porosity and fatigue crack propagation behavior. *Addit. Manuf.* **2021**, *47*, 102324. [CrossRef]
8. Osipovich, K.; Kalashnikov, K.; Chumaevskii, A.; Gurianov, D.; Kalashnikova, T.; Vorontsov, A.; Zykova, A.; Utyaganova, V.; Panfilov, A.; Nikolaeva, A.; et al. Wire-Feed Electron Beam Additive Manufacturing: A Review. *Metals* **2023**, *13*, 279. [CrossRef]
9. Fernandez-Zelaia, P.; Kirka, M.M.; Rossy, A.M.; Lee, Y.; Dryepondt, S.N. Dryepondt, Nickel-based superalloy single crystals fabricated via electron beam melting. *Acta Mater.* **2021**, *216*, 117133. [CrossRef]
10. Lee, D.; Park, S.; Lee, C.-H.; Hong, H.-U.; Oh, J.; So, T.-Y.; Kim, W.-S.; Seo, D.; Han, J.; Ko, S.-H.; et al. Correlation between microstructure and mechanical properties in additively manufactured Inconel 718 superalloys with low and high electron beam currents. *J. Mater. Res. Technol.* **2024**, *28*, 2410–2419. [CrossRef]
11. Karapuzha, A.S.; Fraser, D.; Zhu, Y.; Wu, X.; Huang, A. Effect of solution heat treatment and hot isostatic pressing on the microstructure and mechanical properties of Hastelloy X manufactured by electron beam powder bed fusion. *J. Mater. Res. Technol.* **2022**, *98*, 99–117. [CrossRef]
12. Fortuna, S.; Gurianov, D.; Nikonov, S.; Osipovich, K.; Kolubaev, E. On the Control of Elemental Composition, Macro-, and Microstructure of Directionally Solidified Additive Products from Nickel-Based Alloy. *Metals* **2023**, *13*, 1457. [CrossRef]
13. Astafurov, S.V.; Mel'nikov, E.V.; Astafurova, E.G.; Kolubaev, E.A. Phase composition and microstructure of intermetallic alloys obtained using electron-beam additive manufacturing. Izvestiya. *Ferr. Metall.* **2024**, *67*, 401–408. [CrossRef]

14. Song, D.; Wang, T.; Wei, L.; Jiang, S. Microstructure evolution and functional response of NiTi shape memory alloy manufactured by dual-wire electron beam freeform fabrication. *J. Manuf. Process.* **2024**, *119*, 842–855. [CrossRef]
15. Wahlmann, B.; Körner, C.; Nunn, M. Electron beam wire cladding of nickel alloys and stainless steel on a reactor pressure vessel steel. *Mater. Sci. Eng. A* **2021**, *811*, 141082. [CrossRef]
16. Sasikumar, R.; Kannan, A.R.; Kumar, S.M.; Pramod, R.; Kumar, N.P.; Shanmugam, N.S.; Palguna, Y.; Sivankalai, S. Wire arc additive manufacturing of functionally graded material with SS 316L and IN625: Microstructural and mechanical perspectives. *CIRP J. Manuf. Sci. Technol.* **2022**, *38*, 230–242. [CrossRef]
17. Bölükbaşi, O.S.; Serindağ, T.; Gürol, U.; Günen, A.; Çam, G. Improving oxidation resistance of wire arc additive manufactured Inconel 625 Ni-based superalloy by pack aluminizing. *CIRP J. Manuf. Sci. Technol.* **2022**, *46*, 89–97. [CrossRef]
18. Motwani, A.; Vamsi, P.K.; Puri, Y.; Kumar, A. Post-processing of wire arc additive manufactured Inconel-625 thin structure by electro-discharge machining with TLBO assistance. *Mater. Lett.* **2023**, *348*, 134672. [CrossRef]
19. Zhang, W.; Lei, Y.; Meng, W.; Ma, Q.; Yin, X.; Guo, L. Effect of Deposition Sequence on Microstructure and Properties of 316L and Inconel 625 Bimetallic Structure by Wire Arc Additive Manufacturing. *J. Materi. Eng. Perform.* **2021**, *30*, 8972–8983. [CrossRef]
20. Zheng, Y.; Li, C.; Xie, J.; Yu, Z.; Wang, Y.; Chen, J.; Lu, H.; Yu, C. Effects of thermal history of in-situ thermal management on as-built property heterogeneity of plasma arc additively manufactured Inconel 625. *J. Mater. Res. Technol.* **2023**, *25*, 2654–2675. [CrossRef]
21. Tarasov, S.Y.; Filippov, A.V.; Shamarin, N.N.; Fortuna, S.V.; Maier, G.G.; Kolubaev, E.A. Microstructural evolution and chemical corrosion of electron beam wire-feed additively manufactured AISI 304 stainless steel. *J. Alloys Compd.* **2019**, *803*, 364–370. [CrossRef]
22. Kolubaev, E.A.; Rubtsov, V.E.; Chumaevsky, A.V.; Astafurova, E.G. Micro-, Meso- and Macrostructural Design of Bulk Metallic and Polymetallic Materials by Wire-Feed Electron-Beam Additive Manufacturing. *Phys. Mesomech.* **2022**, *25*, 479–491. [CrossRef]
23. Gan, Z.; Lian, Y.; Lin, S.E.; Jones, K.K.; Liu, W.K.; Wagner, G.J. Benchmark Study of Thermal Behavior, Surface Topography, and Dendritic Microstructure in Selective Laser Melting of Inconel 625. *Integr. Mater. Manuf. Innov.* **2019**, *8*, 178–193. [CrossRef]
24. Yu, L.-J.; Emmanuelle, A. Marquis, Precipitation behavior of Alloy 625 and Alloy 625 plus. *J. Alloys Compd.* **2019**, *811*, 151916. [CrossRef]
25. Liu, X.; Fan, J.; Zhang, P.; Cao, K.; Wang, Z.; Chen, F.; Liu, D.; Tang, B.; Kou, H.; Li, J. Influence of heat treatment on Inconel 625 superalloy sheet: Carbides, γ'', δ phase precipitation and tensile deformation behavior. *J. Alloys Compd.* **2023**, *930*, 167522. [CrossRef]
26. Caleb, O.; Yenusah, C.O.; Ji, Y.; Liu, Y.; Stone, T.W.; Horstemeyer, M.F.; Chen, L.Q.; Chen, L. Three-dimensional Phase-field simulation of γ'' precipitation kinetics in Inconel 625 during heat treatment. *Comput. Mater. Sci.* **2021**, *187*, 110123. [CrossRef]
27. Floreen, S.; Fuchs, G.E.; Yang, W.J. *The Metallurgy of Alloy 625, Superalloys 718,625,706 and Various Derivatives*; Loria, E.A., Ed.; The Minerals, Metals&Materials Society: Pittsburgh, PA, USA, 1994.
28. Singh, J.B. *Alloy 625: Microstructure, Properties and Performance*; Springer: Singapore, 2022. [CrossRef]
29. Hack, H.; Link, R.; Knudsen, E.; Baker, B.; Olig, S. Mechanical properties of additive manufactured nickel alloy 625. *Addit. Manuf.* **2017**, *14*, 105–115. [CrossRef]
30. Luna, V.; Trujillo, L.; Gamon, A.; Arrieta, E.; Murr, L.E.; Wicker, R.B.; Katsarelis, C.; Gradl, P.R.; Medina, F. Comprehensive and Comparative Heat Treatment of Additively Manufactured Inconel 625 Alloy and Corresponding Microstructures and Mechanical Properties. *J. Manuf. Mater. Process.* **2022**, *6*, 107. [CrossRef]